

THE UBIQUITOUS IMPRINT OF RADIATIVE ACCELERATION IN THE MEAN
ABSORPTION SPECTRUM OF QUASAR OUTFLOWSLLUÍS MAS-RIBAS^{1,2,3} AND RENATE MAULAND³*Draft version December 15, 2024*

ABSTRACT

Observational evidence revealing the main mechanisms that accelerate quasar outflows has proven difficult to obtain due to the complexity of the absorption features that this gas produces in the spectra of the emission sources. We build 36 composite outflow spectra, covering a large range of outflow and quasar parameters, by stacking broad ($> 450 \text{ km s}^{-1}$) absorption line (BAL) systems in the spectra of SDSS-III/BOSS DR12 quasars. The two lines of the atomic doublet of C IV, with a separation of $\approx 497 \text{ km s}^{-1}$, as well as those of other species appear well resolved in all the composites. This is in agreement with broad outflow troughs consisting in the superposition of many narrow absorbers. We also report on the ubiquitous detection of the radiative-acceleration signature known as line locking in all the composite outflow spectra. Line locking is driven by the C IV atomic doublet and is visible on the blue side of all the strong absorption transitions. Similar effects from the doublets of O VI, Si IV, or N V, however, are not detected. Our results confirm that radiation pressure is a prevalent mechanism for accelerating outflows in quasars and possibly other environments, and the contribution from only certain species may give insight into the structure of the outflowing gas.

1. INTRODUCTION

Supermassive black holes, with masses as large as billions of times the mass of the Sun, inhabit the center of most, if not all, massive galaxies in the Universe. Despite their small size compared to that of their hosts, these formidable objects can determine the fate of the whole galaxy (Furlanetto & Loeb 2001; Haiman & Bryan 2006; Scannapieco & Oh 2004), as well as contributing to the metal enrichment of the distant intergalactic medium (Cavaliere et al. 2002; Levine & Gnedin 2005).

When the supermassive black holes grow by undergoing episodes of gas accretion they release large amounts of energy and become detectable as active galactic nuclei (AGNs). One of their brightest phases is represented by the so-called quasars, and the energy release, referred to as AGN or quasar feedback, results in powerful winds that can expel material out of the host galaxy (see the reviews by King & Pounds 2015; Harrison 2017).

The origin of quasar feedback may reside in the outflows launched from the innermost regions around the black holes, and that can reach velocities of up to a 10 – 20 % of the speed of light (Moe et al. 2009; Harrison et al. 2018). However, probing the link between fast outflows and quasar feedback is challenging because the mechanisms driving these outflows are still unclear and simulations cannot cover the whole range of physical scales and processes involved (Ciotti et al. 2010; Hopkins & Elvis 2010; Barnes et al. 2018). It is broadly believed that outflows can be accelerated by the pressure that ra-

diation from the quasar exerts on the gas, but questions concerning the overionization, confinement and stability of the outflowing gas have been puzzling astronomers for decades (Williams 1972; Murray et al. 1995; Proga 2007b; Baskin et al. 2014; Proga & Waters 2015; Waters & Proga 2016).

The theory of radiative acceleration in quasar outflows was initially developed by Mushotzky et al. (1972); Scarf (1973); Burbidge & Burbidge (1975); Braun & Milgrom (1989); Arav & Li (1994), and was inspired by that proposed for the ejection of material from massive stars by Milne (1926) and Lucy & Solomon (1970). A common feature appearing in these works is the phenomenon known as line locking, for which absorption systems in the outflow get bound to a fixed relative velocity that coincides with the velocity separation of two atomic transitions, typically the two lines of an atomic doublet. In detail, the outflow absorbs radiation from the quasar and thus gets accelerated. This happens for both line and continuum quasar radiation, although the absorption of line radiation injects a larger boost than the continuum because the flux in the emission lines is the largest. Regarding now the case of an atomic doublet, a region absorbing radiation from both lines of the doublet can suffer a reduction in the acceleration if another region between the first one and the source moves at a lower relative speed coinciding with the doublet separation. In this scenario, the region in the middle also absorbs radiation from the two lines of the doublet in its frame and, given the relative velocity between the two regions, it blocks (absorbs) the flux of the bluest doublet line that was previously available for the front region (reddest line in the frame of the front region). If the back region then increases the speed, the flux-masking decreases and the front region increases the speed accordingly, thus restoring the relative velocity. The acceleration of the front region is thus regulated by the back region, and the two regions get locked at the velocity corresponding to the

¹ Jet Propulsion Laboratory, California Institute of Technology, 4800 Oak Grove Drive, Pasadena, CA 91109, U.S.A.

² California Institute of Technology, 1200 E. California Blvd, Pasadena, CA 91125, U.S.A.

³ Institute of Theoretical Astrophysics, University of Oslo, Postboks 1029, 0315 Oslo, Norway.
lluís.mas-ribas@jpl.nasa.gov

doublet separation.

The observation of line-locking signatures of a given species in the spectra of quasars can therefore confirm the presence of radiative acceleration in the outflows. These observations, however, are not easy due to the complexity of the outflow absorption features, usually broad, and also the difficulties in distinguishing line locking from randomly located absorption components (e.g., Korista et al. 1993).

Absorption due to outflows was first identified as strong and broad absorption lines (BALs) from high-ionization species such as C IV, Si IV or N V, blueshifted from the AGN rest-frame position (Lynds 1967). Nowadays, outflow features are observed in a variety of widths and depths, and line locking from high-ionization species is suggested in a small number of them: Foltz et al. (1987) and Srianand et al. (2002) reported line-locking features in the spectra of one quasar each, and other tentative detections in a few quasars were presented in, e.g., Srianand (2000); Ganguly et al. (2003); Gupta et al. (2003); North et al. (2006); Lu & Lin (2018b). Furthermore, line locking was also detected by Bowler et al. (2014), who analyzed composite spectra of narrow ($\leq 200 \text{ km s}^{-1}$) C IV absorption lines in the spectra of quasars. These authors analyzed narrow absorbers in quasars containing BALs, but they did not use the BALs themselves in order to be able to resolve the C IV doublets and detect the line-locking signatures.

Although the total width of the outflow troughs can be as large as $\sim 30\,000 \text{ km s}^{-1}$, they typically consist in the superposition of narrower features, of the order of a few hundreds of km s^{-1} , the so-called narrow absorption lines (NALs; e.g., Gabel et al. 2006; Lu & Lin 2018a,b). Therefore, it should be possible to obtain the *narrow* outflow absorption spectrum if one centers the broad troughs at a characteristic position when performing the composite spectra (Perrotta et al. 2018). Given this consideration, we conduct here a search for the line-locking signature in 36 composite spectra of broad ($> 450 \text{ km s}^{-1}$) absorption line systems (BALs) representing outflows, and test the prevalence of line locking for multiple properties of the outflows, the quasars, and different atomic species. We assess and present the physical properties of the outflow inferred from the analysis of the composite spectra in our companion paper, Mas-Ribas et al. (in prep).

In § 2 and § 3 we detail the data and methods, respectively, and in § 4 we analyze one of our composite outflow spectra in detail. The C IV, O VI and N V line-locking features are assessed in § 5. We discuss our findings in § 6, before concluding in § 7.

We assume a flat Λ CDM cosmology with the parameter values from Planck Collaboration et al. (2016).

2. DATA

We detail in § 2.1 the quasar spectra used in our calculations, and present the atomic data for the analysis of the absorption lines in § 2.2.

2.1. Quasar Spectra

We use the 297 301 quasar spectra in the twelfth data release of the SDSS-III/BOSS (Eisenstein et al. 2011; Dawson et al. 2013) quasar catalog, DR12Q (Pâris et al. 2017). The characteristics of the SDSS telescope and camera are detailed in Gunn et al. (1998, 2006) and Ross

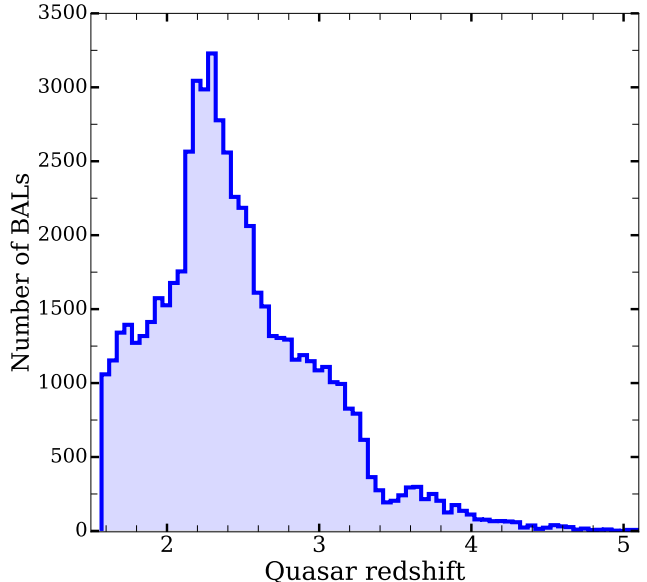


FIG. 1.— Redshift distribution of the DR12Q quasars containing BALs, covering the range $1.5 \lesssim z \lesssim 5.5$.

et al. (2012), and the SDSS/BOSS spectrographs in Smee et al. (2013).

We also use the DR12QBAL catalog, which compiles the individual properties of the C IV absorption troughs with widths $> 450 \text{ km s}^{-1}$ detected in the spectra of the DR12Q quasars. We refer to all these troughs as broad absorption line (BAL) systems for simplicity, regardless of their width or depth. The DR12QBAL catalog contains 63 549 BALs with measurements of their position, width and maximum depth. The position of each BAL was set at the velocity distance from the quasar where the flux within the absorption trough is the minimum, and the BAL width was defined as the velocity range in which the measured normalized quasar flux density (i.e., the flux transmission) is lower than 0.9 (Pâris et al. 2012, 2017). We remove from further analysis 3 677 objects ($\simeq 83\%$ of them with velocity offset from the quasar below $v \sim 400 \text{ km s}^{-1}$) for which the BAL position is measured outside the velocity limits of the corresponding BAL. The composite spectrum of these discarded BALs does not show significant absorption features, indicating that they are false positives and/or severely affected by incorrect velocity offset measurements or noise, and their inclusion in the samples would simply increase the noise at low outflow velocities. Our final sample thus consists of 59 872 BALs.

Figure 1 shows the redshift distribution of the DR12Q quasars containing BALs, which spans the range $1.5 \leq z \leq 5.5$, although only a small number of objects have values above $z \sim 3.3$. The distribution peaks at $z \sim 2.4$, similar to its mean value of $\bar{z} = 2.46$, and decreases rapidly toward both lower and higher values. The *upper panel* in Figure 2 shows the distribution of the velocity offset of the BALs from the quasars, i.e., the outflow velocities, for the final BAL sample. The distribution peaks at around 2000 km s^{-1} and decreases toward higher velocities up to $25\,000 \text{ km s}^{-1}$, with a slight change of slope that flattens beyond $\sim 12\,000 \text{ km s}^{-1}$. For outflow velocities smaller than that of the peak, the decrease in the number of BALs is much steeper, flattening at velocities

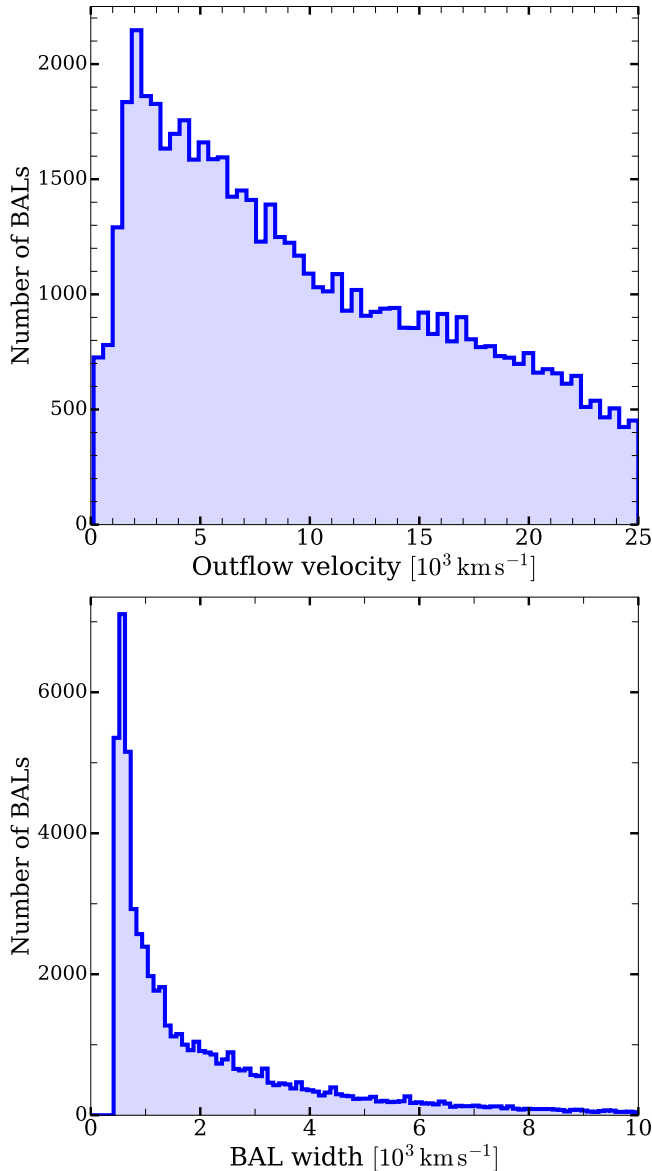


FIG. 2.— *Top panel:* Distribution of outflow velocities, with a minimum value of $\sim 200 \text{ km s}^{-1}$ and a peak at $\sim 2000 \text{ km s}^{-1}$, decreasing toward higher velocities. *Bottom panel:* Distribution of BAL widths, peaking at around 700 km s^{-1} , and decreasing rapidly toward larger widths. The distribution spans from $\sim 300 \text{ km s}^{-1}$ to $25\,000 \text{ km s}^{-1}$, but we only plot values below $10\,000 \text{ km s}^{-1}$ due to the small number of objects above this threshold.

below $\sim 1\,000 \text{ km s}^{-1}$. Overall, this distribution is similar to that obtained by Nestor et al. (2008) who searched for CIV troughs in the quasar spectra of the fourth SDSS data release. The *lower panel* in Figure 2 displays the distribution of BAL widths, which peaks at $\sim 700 \text{ km s}^{-1}$ and decreases rapidly toward higher and lower values. The plot covers the interval $\simeq 300 - 10\,000 \text{ km s}^{-1}$, although a small number of BALs have widths of up to $\sim 25\,000 \text{ km s}^{-1}$.

2.2. Absorption Lines

Table 1 presents vacuum atomic data in the rest frame between 500 \AA and $3\,000 \text{ \AA}$ relevant for the analysis of BAL absorption lines. We have built this catalog by com-

piling data from the database LINETOOLS⁴ (Prochaska et al. 2016) and that of the National Institute of Standards and Technology (NIST⁵; Kramida et al. 2018). This list includes a number of strong absorption lines from highly-ionized species that are typically not observed in interstellar or intergalactic gas studies but that may arise under the extreme conditions of high temperature and strong radiation fields present in quasar outflows. The *first column* in Table 1 denotes each transition and the *second* one its line center in Ångströms (in the vacuum). The corresponding oscillator strengths are shown in the *third column* and the reference source in the *fourth* one.

This table is publicly available in digital format at <https://github.com/lluism/BALs> and the access is open for the community to contribute to its update, correction, and/or extension to make it useful for future studies.

3. METHODS

We detail the calculation of the mean quasar spectrum in § 3.1 and in § 3.2 that of the BAL composite spectrum. Section § 3.3 describes the method for modeling the absorption lines.

3.1. Mean Quasar Spectrum Calculation

We calculate a weighted-mean quasar spectrum that will be used to normalize the spectra for the computation of the BAL composite spectrum, following our procedure in Mas-Ribas et al. (2017). Below we summarize the main steps of this calculation and refer the interested reader to the aforementioned work for details.

In our calculations, we do not consider those spectral pixels affected by the skylines reported by Palanque-Delabrouille et al. (2013). Furthermore, we always correct the flux in the Lyman-alpha forest of the quasar spectra for the redshift-dependent average absorption in this region, using the analytical formula proposed by Faucher-Giguère et al. 2008b (Eq. 7 in Mas-Ribas et al. 2017). For the computation of the mean spectrum we use all the spectra in the DR12Q catalog. This is because the coincident position of BALs in the quasar spectra yields an undesired average broad absorption feature next to the quasar emission lines if only BAL quasars are considered.

The calculation of the mean quasar spectrum is performed as follows: we shift the observed spectra to the rest-frame position of the quasars, considering the visual inspection quasar redshift values in DR12Q, and rebin the flux density and error into an evenly-spaced wavelength array with pixel width of 1 \AA . The spectra are then normalized by dividing them by their corresponding mean flux in the wavelength windows free of emission lines, $1\,300 < \lambda_r/\text{\AA} < 1\,383$ and $1\,408 < \lambda_r/\text{\AA} < 1\,500$. If more than 20% of the pixels in these intervals for one spectrum are not accounted for due to skylines, this spectrum is not used. This constraint rejects less than 10% of the spectra in the catalog. A mean signal-to-noise ratio (S/N) is then calculated for each remaining spectrum j

⁴ <https://linetools.readthedocs.io/en/latest/>

⁵ <https://www.nist.gov/pml/atomic-spectra-database>

TABLE 1 Atomic Data

Transition	λ (Å)	f	Reference
OIII λ 507	507.3910	0.18500	1
NIi λ 533	533.5099	0.29899	1
OII λ 539	539.0855	0.06520	1
NeIV λ 541	541.1270	0.03900	1
NeIV λ 542	542.0730	0.07789	1
CII λ 543	543.2570	0.03489	1
NeIV λ 543	543.8910	0.11599	1
OIV λ 553	553.3300	0.11200	1
OIV λ 554	554.0750	0.22400	1
NeVI λ 558	558.5900	0.09070	1
NeVI λ 558	558.5900	0.09070	1
CII λ 560	560.2394	0.05710	1
NeV λ 568	568.4200	0.09279	1
NeV λ 568	568.4200	0.09279	1
HeI λ 584	584.3300	0.27625	2
CII λ 594	594.8000	0.11699	1
OIV λ 608	608.3980	0.06700	1
MgX λ 609	609.7900	0.08420	1
MgX λ 624	624.9500	0.04100	1
OIV λ 625	625.0000	0.12500	2
OV λ 629	629.7300	0.51499	1
NeVIII λ 632	632.5000	1.35000	2
SVII λ 638	638.6600	0.11700	2
NeVI λ 641	641.2310	0.11800	2
SiI λ 641	641.7670	0.25999	1
OII λ 644	644.1570	0.11100	2
SVI λ 648	648.6260	0.10400	2
SIV λ 657	657.3280	1.13000	2
SIV λ 661	661.4430	1.02000	2
SIII λ 680	680.6800	1.38000	2
SIII λ 681	681.4700	0.06830	1
SIII λ 683	683.5860	1.34000	2
NIII λ 684	684.9960	0.13500	1
NIII λ 685	685.8200	0.32000	2
SIII λ 698	698.7310	0.78299	1
OIII λ 702	702.3320	0.13699	1
SIII λ 724	724.2890	0.35199	1
SIV λ 744	744.9070	0.25099	1
NV λ 748	748.1950	1.04000	2
SIV λ 748	748.4000	0.50000	1
SIV λ 749	749.2520	0.62300	2
NIII λ 763	763.3400	0.08200	1
SIII λ 763	763.6570	0.39800	1
SIII λ 764	764.4200	0.79500	1
NIIV λ 765	765.1480	0.61599	1
SIII λ 765	765.6930	1.19000	1
NeVIII λ 770	770.4090	0.10300	1
NeVIII λ 780	780.3240	0.05050	1
SV λ 786	786.4700	1.36000	2
OIV λ 787	787.7110	0.11100	1
OI λ 791	791.9732	0.04639	1
SIV λ 809	809.6680	0.10400	1
SIV λ 815	815.9450	0.08500	2
OII λ 832	832.7572	0.04439	1
OIII λ 832	832.9270	0.10700	1
OII λ 833	833.3294	0.08860	1
OII λ 834	834.4655	0.13199	1
FeII λ 844	844.2880	0.06840	1
CII λ 858	858.0918	0.01300	1
FeII λ 859	859.7230	0.11500	1
FeII λ 861	861.0000	0.13100	2
PIV λ 877	877.4760	1.60000	2
OI λ 877a	877.7983	0.01970	1
OI λ 877b	877.8787	0.05889	1
SIII λ 883	883.4000	9.49000	2
Fev λ 887	887.2560	0.11000	2
SIII λ 889	889.7228	0.04340	1
SiI λ 906	906.8850	0.21000	1
PIII λ 913	913.9683	0.20300	1
NIi λ 915	915.6131	0.15900	1
PIII λ 917	917.1178	0.40400	1
OIV λ 921	921.3660	0.11200	2
OIV λ 923	923.3670	0.14100	2
SVI λ 933	933.3780	0.43700	1
HI λ 937	937.8034	0.00780	1
SVI λ 944	944.5230	0.21500	1
CI λ 945	945.1910	0.15200	1

TABLE 1 – Continued

Transition	λ (Å)	f	Reference
OI λ 948	948.6855	0.00631	1
HI λ 949	949.7430	0.01395	1
PIV λ 950	950.6600	1.60000	2
NIIV λ 955	955.3350	0.13310	2
SV λ 957	957.6900	1.02000	2
NI λ 963	963.9903	0.01240	1
NI λ 964	964.6256	0.00790	1
HI λ 972	972.5367	0.02901	1
CIII λ 977	977.0201	0.75700	1
Fev λ 988	988.6230	0.79000	2
OI λ 988	988.7734	0.04650	1
NIII λ 989	989.7990	0.12300	1
SIII λ 989	989.8731	0.17100	1
Fev λ 997	997.6520	0.83000	2
SIII λ 1012	1012.495	0.04380	1
SIII λ 1020	1020.698	0.01680	1
HI λ 1025	1025.722	0.07914	1
AlIV/Fev λ 1028 ^a	1028.100	—	2
OVI λ 1031	1031.926	0.13250	1
CII λ 1036	1036.336	0.11800	1
OVI λ 1037	1037.616	0.06580	1
OI λ 1039	1039.230	0.00907	1
FeII λ 1055	1055.261	0.00750	1
MgIV λ 1061	1061.722	0.31100	2
SIV λ 1062	1062.664	0.04940	1
SIV* λ 1073	1073.508	0.00390	2
NIIV λ 1078	1078.710	0.29800	2
FeII λ 1081	1081.874	0.01260	1
NIi λ 1083	1083.993	0.11100	1
FeII λ 1096	1096.876	0.03200	1
FeII λ 1112	1112.048	0.00620	1
CI λ 1112	1112.269	0.01610	1
PV λ 1117	1117.977	0.47200	1
FeII λ 1121	1121.974	0.02020	1
CI λ 1122	1122.437	0.00511	1
SIIV λ 1122	1122.490	0.80000	2
FeIII λ 1122	1122.524	0.05440	1
FeII λ 1125	1125.447	0.01600	1
CrV λ 1127	1127.630	0.82000	2
PV λ 1128	1128.007	0.23300	1
SIIV λ 1128	1128.340	0.72500	2
CI λ 1129	1129.195	0.00771	1
FeII λ 1133	1133.665	0.00550	1
NI λ 1134a	1134.165	0.01460	1
NI λ 1134b	1134.414	0.02870	1
NI λ 1134c	1134.980	0.04160	1
SIII λ 1140	1140.550	1.15000	2
FeII λ 1143	1143.226	0.01920	1
FeII λ 1144	1144.937	0.08300	1
CI λ 1158	1158.324	0.00655	1
NeVIII λ 1165	1165.000	1.68000	2
CIII* λ 1175	1175.260	0.72400	2
FeII λ 1180	1180.426	0.11000	2
FevII λ 1180	1180.823	0.21000	2
SIII λ 1190	1190.203	0.02370	1
SIII λ 1190	1190.415	0.29200	1
CI λ 1193	1193.030	0.04090	1
SIII λ 1193	1193.289	0.58200	1
SIII λ 1194	1194.500	0.73700	2
MnII λ 1197	1197.184	0.21700	1
MnII λ 1199	1199.391	0.16900	1
NI λ 1199	1199.549	0.13200	1
NI λ 1200	1200.223	0.08690	1
NI λ 1200b	1200.709	0.04320	1
SIII λ 1206	1206.500	1.63000	1
HI λ 1215	1215.670	0.41640	1
SIII λ 1235	1235.430	1.90000	2
NV λ 1238	1238.821	0.15600	1
NV λ 1242	1242.804	0.07770	1
SIi λ 1250	1250.578	0.00543	1
SIi λ 1253	1253.805	0.01090	1
SIII λ 1260	1260.422	1.18000	1
SIII λ 1264	1264.730	1.09000	2
MgIII λ 1274	1274.830	0.10300	2
CI λ 1276	1276.482	0.00589	1
CI λ 1277	1277.245	0.08530	1
SIIII λ 1294	1294.540	0.02240	2

TABLE 1 – Continued

Transition	λ (Å)	f	Reference
Siv λ 1294	1294.592	0.12600	2
SiIII λ 1296	1296.730	0.53700	2
OI λ 1302	1302.168	0.04800	1
SiII λ 1304	1304.370	0.08630	1
MgIV λ 1307	1307.900	0.14200	2
NiII λ 1317	1317.217	0.14599	1
CrI λ 1328	1328.833	0.07580	1
CrII λ 1334	1334.532	0.12800	1
Siv λ 1335	1335.108	0.06000	2
CrII λ 1335	1335.708	0.11500	2
SiIII λ 1341	1341.470	0.24200	2
MgIV λ 1356	1356.108	0.20200	2
SiIII λ 1361	1361.600	0.49100	2
NiII λ 1370	1370.132	0.07690	1
Siv λ 1393	1393.755	0.52399	1
Siv λ 1402	1402.770	0.25999	1
SvI λ 1423	1423.845	0.18100	2
MgIV λ 1425	1425.597	0.68000	2
MgIV λ 1427	1427.710	0.61200	2
SiIII λ 1436	1436.170	0.72300	2
MgIV λ 1447	1447.395	0.43700	2
NiII λ 1454	1454.842	0.03230	1
SiIII λ 1500	1500.240	0.91100	2
SiIII λ 1501	1501.870	0.99100	2
SiII λ 1526	1526.707	0.12700	1
CrV λ 1548	1548.204	0.18999	1
NV λ 1549	1549.336	0.47300	2
CrV λ 1550	1550.770	0.09520	1
CrI λ 1560	1560.309	0.07740	1
SiI λ 1589	1589.174	0.05040	1
FeII λ 1608	1608.451	0.05770	1
CrI λ 1656	1656.928	0.14900	1
AlII λ 1670	1670.788	1.74000	1
MgIV λ 1683	1683.000	0.31900	2
MgIV λ 1701	1701.262	0.47500	2
NiII λ 1703	1703.411	0.00600	1
Ov λ 1707	1707.996	1.14000	2
NiII λ 1709	1709.604	0.03240	1
NiII λ 1741	1741.553	0.04270	1
NiII λ 1751	1751.915	0.02770	1
NiII λ 1773	1773.949	0.00621	1
NiII λ 1804	1804.473	0.00716	1
MgI λ 1827	1827.935	0.02420	1
NiIII λ 1854	1854.150	0.34000	2
AlIII λ 1854	1854.716	0.57499	1
AlIII λ 1862	1862.789	0.28600	1
NiII λ 1907	1907.990	0.79200	2
Siv λ 1908	1908.942	0.17900	2
NeVIII λ 1931	1931.000	2.01000	2
ZnII λ 2026	2026.137	0.50100	1
CrII λ 2056	2056.256	0.10300	1
CrII λ 2062	2062.234	0.10499	1
ZnII λ 2062	2062.664	0.25299	1
CrII λ 2066	2066.161	0.06979	1
FeII λ 2344	2344.213	0.11400	1
FeII λ 2374	2374.461	0.03130	1
FeII λ 2382	2382.765	0.32000	1
Pv λ 2425	2425.140	1.10000	2
MnII λ 2576	2576.877	0.36100	1
FeII λ 2586	2586.650	0.06910	1
MnII λ 2594	2594.499	0.28000	1
FeII λ 2600	2600.172	0.23900	1
MnII λ 2606	2606.462	0.19800	1
Niv λ 2646	2646.440	1.17000	2
Niv λ 2646b	2646.970	1.09000	2
Niv λ 2647	2647.750	1.11000	2
MgII λ 2796	2796.354	0.61550	1
MgII λ 2803	2803.531	0.30580	1
MgI λ 2852	2852.964	1.73000	1

Transitions arising from excited metastable states are denoted by an asterisk.

References: (1) LINETOOLS (2) NIST.

^a Uncertain blend of atomic transitions. The average wavelength was handpicked for fitting purposes.

as

$$S/N_j = \frac{\sum_i f_{ij}/N_j}{(\sum_i e_{ij}^2/N_j)^{1/2}}, \quad (1)$$

where e_{ij} is the uncertainty for the flux f_{ij} at the pixel i and N_j is the number of pixels within the above wavelength windows intervening in the summation. Those spectra with $S/N < 1$ are discarded from further calculations. This threshold eliminates around 22% of the remaining spectra from the calculations. Finally, the mean S/N values are used for assigning to each quasar spectrum a weight of the form

$$w_j = \frac{1}{S/N_j^{-2} + \sigma^2}, \quad (2)$$

where $\sigma = 0.1$ limits the potential excessive contribution from spectra with very high S/N . In Mas-Ribas et al. 2017 we tested that small variations around this value do not alter our results, and we therefore use the same quantity. The final mean quasar spectrum is then computed as a weighted mean using the aforementioned weight values.

Figure 3 shows the difference between the spectrum considering all the DR12Q quasar spectra (*black line*), and only those containing BALs (*red line*). A broad absorption trough is visible to the left of the emission lines of species with the highest opacities, i.e., CIV, NV, Ly α and OVI, in the BAL-only spectrum. The use of this biased mean spectrum would result in the underestimation of the true line equivalent widths. We have checked that including the quasars containing BALs to the total quasar sample for this calculation does not affect the resulting mean quasar spectrum. A similar mean spectrum, except for the lack of corrections on the average absorption of the Lyman-alpha forest, is illustrated in Figure 3 of Mas-Ribas et al. (2017), and a movie showing the build up of the mean quasar spectrum with an increasing number of spectra is publicly available at https://github.com/lluism/DLA_movies.

We have tested the impact on our results of using an individual mean spectrum for every quasar spectrum, derived from the spectra of its nearest neighbors, instead of our mean quasar calculation. In detail, the mean spectrum for each quasar containing BALs is obtained by computing the mean spectrum of its forty BAL-free nearest neighbors among the entire DR12Q catalog, similar to the procedure used by Davies et al. (2018). Using the mean spectra from the nearest-neighbor approach yields BAL composite spectra slightly less noisy redward the CIV absorption doublet compared to using the mean of all the quasars. This is because the individual mean, i.e., from the nearest neighbors, matches the quasar spectra better than the overall mean. However, the noise for the nearest-neighbor case is significantly larger at short wavelengths, especially in the Lyman-alpha forest, since not all the spectra in the DR12Q catalog cover the region below ~ 1500 Å in the quasar rest-frame. If one considers only the spectra that covers the entire forest region ($\gtrsim 912$ Å) then the number of spectra and candidate neighbors is reduced and the resulting BAL composite does not show a significant improvement compared to using our mean spectra. We therefore conclude that our mean quasar spectrum method is adequate for our

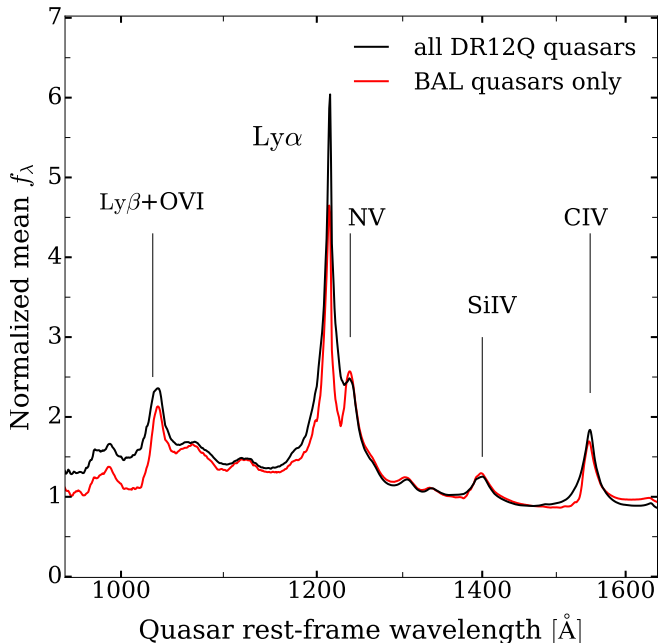


FIG. 3.— Mean quasar spectrum considering all DR12Q quasars (black line) and only those containing BALs (red line). The average BAL absorption features of the elements with highest opacities, such as CIV, NV, Ly α and OVI, are visible on the left part of the respective emission lines in the red spectrum. The horizontal axis is logarithmically spaced for visualization.

calculations.

3.2. BAL Composite Spectra Calculation

We compute the composite rest-frame outflow spectrum as a weighted mean, now only using the quasar spectra that contain BALs, and centering these spectra at the position of the minimum flux within the BAL troughs as given in DR12QBAL. Perrotta et al. (2018) recently stacked BAL features in high-resolution spectra and they found that centering the spectra at the position of the deepest (minimum flux) CIV component yields the best alignment between CIV and the other absorption features, especially those of low-ionization species. In our case, given the low resolution of the BOSS spectra, the position of the minimum flux can be determined with higher accuracy than the limits of the troughs or other points, which in turn results in more precise (narrower) absorption profiles. Indeed, our stacks do not resolve the two lines of the CIV doublet and show much broader absorption features if we center the spectra at the centroid of the troughs, or at the minimum or maximum BAL limits. This test suggests that the minimum flux position mostly has a physical origin and that the effect of noise is small. We elaborate further on the impact of choosing the minimum-flux position on our results in § 6.1.

The redshift of the BALs is computed using the velocity offset from the quasar given in the DR12QBAL catalog, i.e., the BAL position, and the expression

$$\frac{v}{c} = \frac{(1+z_q)^2 - (1+z_{\text{BAL}})^2}{(1+z_q)^2 + (1+z_{\text{BAL}})^2}. \quad (3)$$

Here v and c are the BAL position and the speed of light respectively, and z_{BAL} and z_q denote the redshifts of the BAL and the quasar, respectively. We then rebin each

BAL spectrum into an evenly-spaced array of pixel width $d\lambda = 0.3 \text{ \AA}$, similar to the maximum BOSS pixel resolution ($\approx 69 \text{ km s}^{-1}$ in velocity space), and normalize them with the corresponding normalization factor obtained in the mean spectrum calculation. Next, the normalized spectra are divided by the mean quasar spectrum, shifted and rebinned to the new BAL wavelength array, to eliminate the quasar footprint and obtain the individual BAL absorption spectra. The final BAL composite spectrum results from computing the weighted mean of these individual BAL absorption spectra, where the weighting factors are the weights obtained for every spectrum in the mean quasar calculation. At the end of these calculations, the composite spectra present a residual offset of $\approx 200 \text{ km}^{-1}$. This is because we used the visual-inspection redshift for the quasars, while the BAL positions are determined from the CIV emission lines (see the peak separation between the redshift distributions from visual inspection and CIV in Figure 7 of Pâris et al. 2017). We simply correct for this offset by shifting our composite spectra, given the higher accuracy of the redshift from visual inspection ($\approx 265 \text{ km}^{-1}$ at $z = 2.4$) than that from CIV, and note that this offset value is small compared to the accuracy of the redshifts and their dispersion (section 4.5 in Pâris et al. 2017).

We build 36 outflow composite spectra drawn from subsamples of the overall BAL catalog, all computed as described above. We divide the outflow velocity range in nine bins and consider two additional subsamples for low velocities. The BAL width range is divided in five samples and the BAL minimum velocity in seven. The quasar redshift and magnitude ranges are divided in six bins each. Together with the stack of all BALs in the catalog, these subsamples are detailed in Table 2. The *first column* lists the selection criteria to build each subsample, where *BAL min. velocity* is the minimum velocity of each BAL trough, and the bottom group is parameterized using the absolute i -band magnitude at $z = 2$ of the quasars as reported in DR12Q (Pâris et al. 2017). The *second column* in Table 2 quotes the mean value for each selection parameter, and the *third one* the values of the intercept used for the calculation of the a parameters in the absorption profile (Eq. 4 and § 3.3.3). The *fourth column* denotes the number of spectra considered for the composite of each subsample. We publicly release our composite spectra with their analysis in our companion paper (Mas-Ribas et al, in prep).

3.3. Line Profile fitting

We describe the wavelength ranges considered for the modeling of the absorption lines and the continua in § 3.3.1, the formula for the absorption profile fitting in § 3.3.2, and the computation of the absorption width in § 3.3.3. For the modeling of the absorption lines we consider the set of 223 atomic transitions listed in Table 1, although not all of them are detected in all our stacks.

3.3.1. Line Windows and Local Continua

The first step towards obtaining a reliable fit to the absorption profiles is to renormalize the BAL composite spectra. This modification is required because the impact of neighboring BAL features and/or the Lyman-alpha forest in some cases results in absorption-free spectral regions that deviate significantly from the unity

TABLE 2
BAL SAMPLES

Selection criteria	Mean	$n(\text{\AA})$	No. BALs
all		0.437	59 872
Outflow velocity (km s^{-1})			
$v < 200$	139	0.335	185
$v < 350$	264	0.331	3 167
$v < 650$	315	0.254	4 355
$350 \leq v < 650$	452	0.278	1 188
$650 \leq v < 1 500$	1 122	0.291	2 278
$1 500 \leq v < 3 000$	2 233	0.387	6 706
$3 000 \leq v < 5 000$	3 980	0.444	7 727
$5 000 \leq v < 8 000$	6 426	0.462	10 183
$8 000 \leq v < 13 000$	10 330	0.439	12 488
$13 000 \leq v < 17 500$	15 208	0.354	9 075
$v > 17 500$	20 867	0.302	10 737
BAL width (km s^{-1})			
$v < 560$	508	0.227	11 250
$560 \leq v < 708$	629	0.349	8 420
$708 \leq v < 1 260$	951	0.305	13 488
$1 260 \leq v < 2 240$	1 704	0.381	10 266
$v \geq 2 240$	5 179	0.560	20 125
BAL min. velocity (km s^{-1})			
$v < 300$	128	0.423	2 574
$300 \leq v < 2 300$	1 236	0.431	10 713
$2 300 \leq v < 5 300$	3 694	0.381	10 661
$5 300 \leq v < 9 000$	7 113	0.352	10 356
$9 000 \leq v < 13 500$	11 183	0.400	10 570
$13 500 \leq v < 18 500$	15 953	0.409	10 059
$v \geq 18 500$	21 186	0.463	8 630
Quasar redshift			
$z < 1.95$	1.77	0.449	10 580
$1.95 \leq z < 2.20$	2.09	0.455	10 584
$2.20 \leq z < 2.37$	2.28	0.455	10 812
$2.37 \leq z < 2.60$	2.48	0.414	10 591
$2.60 \leq z < 3.00$	2.79	0.452	10 880
$z \geq 3.00$	3.38	0.461	10 098
Quasar magnitude (mag)			
$-25.0 \leq M_i < -22.0$	-24.6	0.522	10 972
$-25.5 \leq M_i < -25.0$	-25.3	0.482	10 912
$-26.0 \leq M_i < -25.5$	-25.8	0.428	12 932
$-26.5 \leq M_i < -26.0$	-26.2	0.415	12 020
$-27.0 \leq M_i < -26.5$	-26.7	0.387	8 949
$-30.0 \leq M_i < -27.0$	-27.5	0.383	7 749

transmission value in the final spectra. We renormalize each BAL composite spectrum by dividing it by a pseudo-continuum. This is computed via smoothing the composites with a Gaussian kernel of width $\sigma_G = 10$ pixels, showing no substantial differences for other values within the range $5 \leq \sigma_G \leq 15$. For the smoothing, we disregard the wavelength ranges $-1.7 \leq (\lambda - \lambda_c)/\text{\AA} \leq 1.0$ around the absorption lines, where λ_c denotes the line center. The ranges are asymmetrically centered around the lines to account for the presence of the line-locked component in the low-wavelength side of each absorption feature. Despite this correction, the final absorption spectrum is still not completely flat around the absorption lines in some cases. For this reason we will use a local continuum over the absorption lines for the profile fitting as described below.

The absorption profiles are modeled in a wavelength window with a half width of 4\AA on each side of the line center, plus an additional extent of 500 km s^{-1} on the low-wavelength limit to account for the presence of the line-locking component. This window size is large

enough to cover the lines and their line-locked components in all our composite spectra. When two or more line windows overlap we consider a single window spanning from the lowest to the highest limit of the intervening windows, and the profiles of all the lines within this range are modeled at the same time. This approach results in the simultaneous modeling and measurement of up to five absorption lines in general. In order to measure the two lines of the OVI $\lambda\lambda 1031, 1037$ doublet together, we will consider six features, and in two other cases we obtain a window containing ten lines, in the wavelength range around $\sim 1125 \text{\AA}$ and the one around $\sim 1195 \text{\AA}$. We simply divide both ranges in two parts containing five lines each and treat them as separate features. Most lines in these ranges are weak and their precise measurement does not impact our findings so we do not attempt more complex computations.

The local continuum over each absorption feature is computed by fitting a linear regression to the flux pixels next to the absorption window. We consider the BAL transmission pixels beyond the limits of the line (lines) window up to a distance of 9\AA on both sides from the line center (or the minimum and maximum line centers for the case of multiple lines). We require a minimum total number of 15 pixels in these ranges. This value is chosen to reduce the impact of spurious flux pixels while representing the regions near the absorption lines. If the total number of pixels in the two ranges is smaller, due to pixels not being considered as they belong to neighboring line windows or are affected by skylines, both ranges are recursively enlarged by 0.4\AA until the minimum number is reached.

3.3.2. Profile Estimator

The presence of the line-locking component in our outflow spectra requires, for every absorption line, the joint fit of two features: the line itself and the line-locked counterpart. For clarity, we will refer to these two components as *line* and *line-locking* from here onward, and we will account for the two contributions in all our measurements.

We fix the center of the line-locking considering that $v_c - v_{ll} \equiv \Delta_v = -497 \text{ km s}^{-1}$, where v_c and v_{ll} are the positions of the line and line-locking in velocity space, respectively, and the value corresponds to the separation between the two lines of the CIV $\lambda\lambda 1548, 1550$ doublet. We choose this value because the stacking of CIV troughs results in the enhancement of the CIV line-locking feature, while it dissipates the contribution from other doublets. We have tested that variations of $\leq 15 - 20 \text{ km s}^{-1}$ around the nominal CIV separation value (corresponding to a $\sim 22 - 29\%$ of the pixel size) generally do not produce significant differences in the fits.

We perform a least-squares fit to each line and line-locking pair assuming a profile of the form

$$F_\lambda = C_\lambda \exp \left[-b \exp \left(\frac{-(\lambda - \lambda_c)^2}{2a^2} \right) - d \exp \left(\frac{-(\lambda - \lambda_{ll})^2}{2a^2} \right) \right], \quad (4)$$

where the position of the line-locking in wavelength space is obtained with the relation $\lambda_{ll} = \lambda_c (1 + \Delta_v/c)$, noting the negative sign of Δ_v . The parameter C_λ in Eq 4

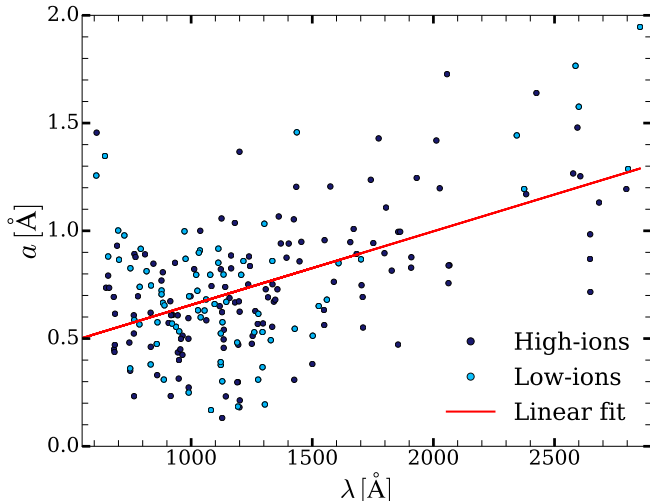


FIG. 4.— Mean values of the a parameters with wavelength, computed from the 34 composite BAL spectra detailed in the main text. There are no apparent differences between the trends for low- (light blue) and high-ionization (dark blue) species, and a general increase of a with wavelength is visible although with a large scatter. The red line denotes the linear fit that yields the slope value $m = 3.4 \times 10^{-4}$, used to obtain the a parameter in the individual stacks.

represents the local continuum at a wavelength λ in the renormalized rest-frame BAL composite spectrum, and b , d and a are free parameters. The a parameter is set to be the same for the line and line-locking, which yields a substantial improvement of the fits, especially when multiple features are fitted at the same time and degeneracies between them can occur. Furthermore, we do not observe significant differences between the paired a parameters when they are allowed to be different. However, the a parameter is related to the width of the absorption features, which is mostly driven by the spectrograph resolution in the BOSS spectra, except for the broadest features. Because of this dependence on resolution, differences between the widths of line and line-locking, not detectable in our spectra, can exist. It is important that future (higher-resolution) analyses revisit these values as the line width carries relevant information on the kinematic properties of the media. Finally, we require that the ratio between the depths of line and line-locking, i.e. d/b , in our measurements are the same for the members that pertain to an atomic doublet.

3.3.3. Fixing the Line Widths

In practice, we fix the value of the parameter a in our calculations, taking into account its dependence on the spectrograph resolution mentioned above and the evolution of the latter with wavelength. This approach yields a reduction in the number of free parameters and, in turn, an improvement of the fits to the absorption profiles.

We first parametrize the evolution with wavelength in 34 of our BAL composite spectra to cover a broad range of BAL parameter values and to assess possible dependences of the evolution on these parameters. We consider the total sample, the six spectra for the subsamples in BAL redshift, the six for the BAL width, four for the low velocity limit of BALs, the six for quasar magnitudes, and the eleven for the outflow velocities, all of them detailed in Table 2. We fit all the features in Ta-

ble 1 for each of these spectra, with the a parameter for every line and line-locking pair allowed to be free, and keep the a values when the fit exists (we consider that a fit does not exist and ignore its outcome when it returns unphysical, i.e., null or negative, values for some of the parameters). An increase of the a parameter with wavelength is apparent in all cases. However, a large scatter in the individual a values, partially driven by degeneracies between blended absorbers and by high noise in the spectra of some stacks that especially affects the weakest features, does not enable us to constrain the wavelength dependence with accuracy in the individual stacks. Thus, we decide to parameterize the slope of the evolution with wavelength by using the mean of the a values from the 34 subsamples, which is consistent with the lack of visible differences in the evolutions between subsamples or between low- and high-ionization species. We finally fit a linear regression to these mean values and use its slope of $m = 3.4 \times 10^{-4}$ for the computation of the a parameter in all the composite subsamples. This slope is similar to the one we obtained for DLAs in Mas-Ribas et al. 2017 (2.3×10^{-4}), indicating that the evolution is mostly driven by the values of the wavelength and not by physical effects specific of outflow environments.

Figure 4 displays the mean value of the a parameters with wavelength, computed using the 34 composite spectra of the subsamples described above. A general increase of a with wavelength is visible although with significant scatter, and there are no apparent differences between low- (light blue) and high-ionization (dark blue) species. The red line denotes the linear fit to the data that yields the slope value of $m = 3.4 \times 10^{-4}$.

With the value of the slope now fixed, we again apply a linear regression to the a values of each subsample to obtain the individual best-fit value of the intercept, n . In this case, we only consider the a parameters of the strong transitions H I $\lambda 1215$, N V $\lambda 1238$, N V $\lambda 1242$, Si IV $\lambda 1393$, Si IV $\lambda 1402$, and C IV $\lambda 1548$, where the a parameters are measured with the highest precision. In all cases we visually inspect the fits to these absorption features and discard those that appear dubious or affected by contaminants. The best-fit values of the n parameters for each subsample are reported in Table 2. Finally, the value of the a parameter for an absorption feature at wavelength λ can be obtained as

$$a = 3.4 \times 10^{-4} \lambda + n, \quad (5)$$

where n takes on the values in Table 2 for each spectrum, and the parameters are in units of Ångstrom.

4. DISSECTION OF A BAL COMPOSITE SPECTRUM

Figure 5 displays the BAL composite spectrum resulting from the subsample of BALs with outflow velocities within the range $1500 \leq v < 3000 \text{ km s}^{-1}$. The light blue color represents the transmitted flux regions and the dark blue highlights the absorbed ones where the transmission falls below the unity value. Note that the scales of the axes for each range are set independently for visualization purposes.

This spectrum was renormalized using a pseudo-continuum as described in § 3.3.1, but the local continua around the absorption features used for the calculation of the equivalent widths were not applied since they depend on each feature. Regions with transmission above

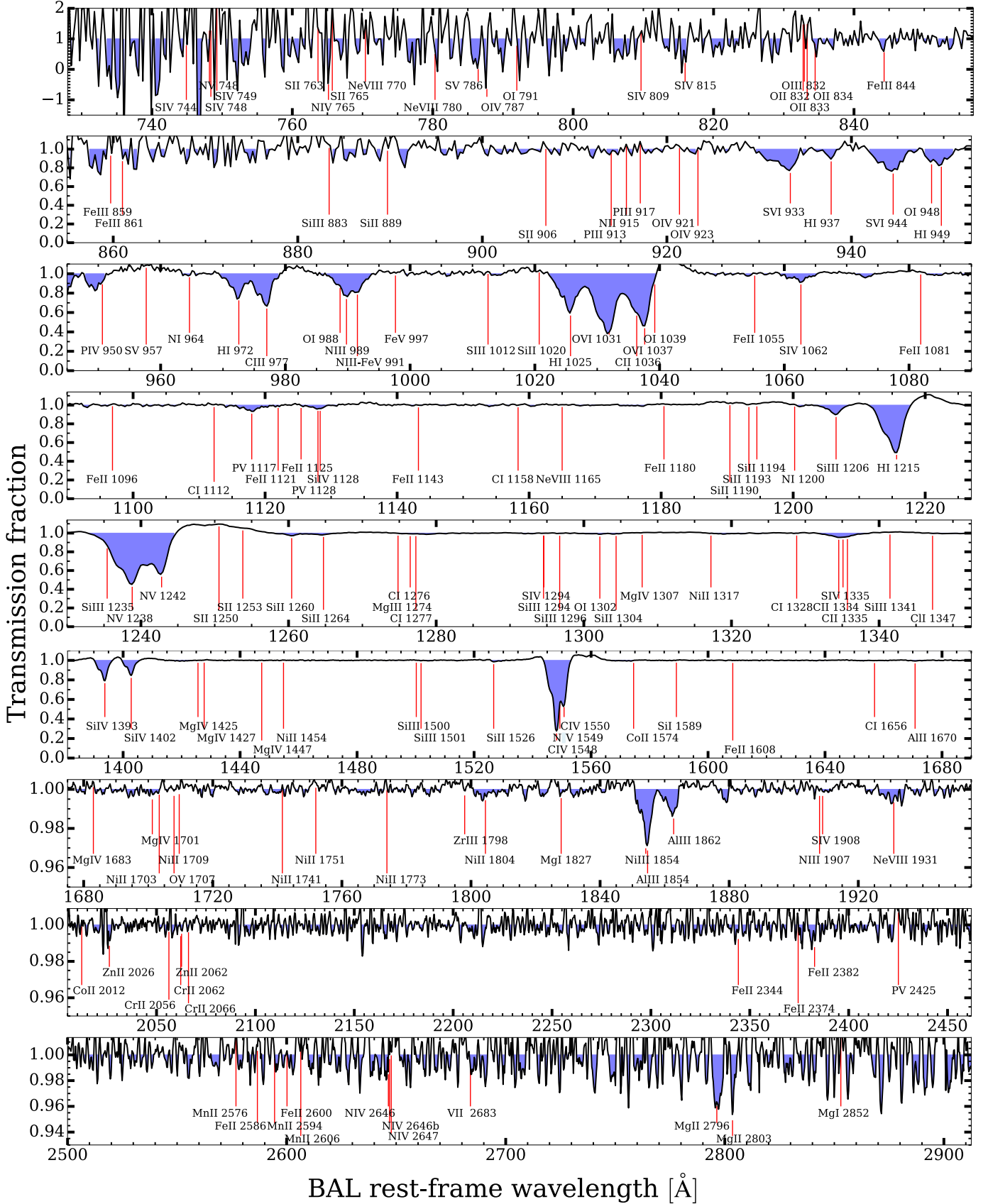


FIG. 5.— Outflow composite spectrum for the subsample with outflow velocities in the range $1500 \leq v < 3000 \text{ km s}^{-1}$. The *light blue* color represents the transmitted quasar flux and the *dark blue* the absorbed regions with transmission below the unity value. Around 150 of the absorption features in Table 1 are labeled for identification, and the axes in each range are independently scaled for visualization. The line-locking component is visible in the low-wavelength side of the strongest absorption features. This spectrum was normalized for visualization by using a simple smooth continuum on the original spectrum. A flux excess next to some of the strongest absorption features arises from the differences between the mean quasar spectrum used for the normalization of the composites and the individual quasar spectra.

the unity, visible on the right-hand side of the absorption features of $\text{O I } \lambda 1039$, $\text{H I } \lambda 1215$, $\text{N V } \lambda 1242$ and $\text{C IV } \lambda 1550$, appear due to differences between the mean quasar spectrum used for the normalization of the composites and the individual quasar spectra. In general, this flux excess indicates that the mean quasar spectrum presents weaker emission lines than those in the individual quasars. However, the effect of weighting the spectra also causes this effect because the higher S/N is typically related to the brighter quasars which, in turn, have weaker emission lines due to the Baldwin effect (Baldwin 1977, see Figure 3 in Mas-Ribas et al. 2017 and the associated text for details). We do not apply further corrections as this effect does not impact our results concerning the line locking, and the equivalent widths of the lines are well fitted given the fix value of their widths.

We have labeled around 150 atomic transitions from Table 1, a number of them identifiable deep into the Lyman-alpha forest region down to $\sim 750 \text{ \AA}$. The strongest features are the well-resolved doublets of the high-ionization species $\text{S VI } \lambda \lambda 933, 944$, $\text{O VI } \lambda \lambda 1031, 1037$, $\text{N V } \lambda \lambda 1238, 1242$ and $\text{C IV } \lambda \lambda 1548, 1550$. These ions represent the typical effect from the strong radiation field affecting the outflow in general. However, other transitions of high- and low-ionization species are clearly visible, such as the first five hydrogen Lyman series lines from Lyman-alpha down to Lyman-epsilon, i.e., $\text{H I } \lambda 937$, and $\text{C III } \lambda 977$, $\text{N III } \lambda 989$, $\text{Si III } \lambda 1206$, and the doublets $\text{P V } \lambda \lambda 1117, 1128$, $\text{Si IV } \lambda \lambda 1393, 1402$, $\text{Al III } \lambda \lambda 1854, 1862$ and $\text{Mg II } \lambda \lambda 2796, 2803$. We have also labeled several transitions of the low-ionization species N II , Fe II , O I , Si II , C II and Cl , barely visible in Figure 5, but detectable in other composite spectra where the low-ionization absorbers are stronger than in the current case. We find no evidence for the presence of molecular H_2 features, although the line-locking component on the left-hand side of the absorption lines may overlap and mask the molecular hydrogen signatures. Finally, we emphasize the tentative detections of $\text{Ne VIII } \lambda 1931$ and the long-wavelength line of the $\text{Ne VIII } \lambda \lambda 770, 780$ doublet. We study the physical properties of the outflows by analyzing this and the other composite spectra in our companion paper, Mas-Ribas et al. (in prep.).

An absorption feature on the low-wavelength side of all lines, and blended with them, is clearly visible for the case of the strongest transitions in Figure 5. We identify this feature as the C IV line-locking component of the corresponding lines and analyze it in more detail below.

5. LINE LOCKING

We analyze the characteristics and nature of the line-locking components below. In § 5.1 we discuss the C IV-driven features visible in our spectra, and search for signatures of O VI and N V in § 5.2.

5.1. C IV Line Locking

Figure 6 illustrates the fits to three of the strongest absorption features in the spectrum of Figure 5. From left to right, the panels cover the approximate wavelength ranges $1\,020\text{--}1\,040 \text{ \AA}$, $1\,230\text{--}1\,250 \text{ \AA}$, and $1\,540\text{--}1\,560 \text{ \AA}$. The *colored solid curves* denote the fit to the individual lines and the *dashed curves* are the fits to the correspond-

ing line-lockings, following the same color code. The *magenta curves* represent the total fit in each panel, and the local continua are visible as *straight lines* over the features, where the colors simply result from the superposition of the individual curves and have no meaning. The C IV line-locking components at 497 km s^{-1} from the corresponding lines are clearly visible. This occurs for any absorption feature visible beyond the noise in all our composite spectra, regardless of the species or the ionization state, as expected from the theory of radiative acceleration in quasar outflows (e.g., Arav & Li 1994; Arav & Begelman 1994).

In cases of blending or weak absorption features, the fit is sometimes better without the line-locking (or line) but we attribute this result to degeneracies between overlapping transitions or to the effect of noise, respectively, and not to physical causes. This is the case of the weak N V $\lambda 1549$ feature in the right panel of Figure 6, where the best fit is reached considering the line-locking but no line. The degeneracy of the N V $\lambda 1549$ line with the two lines of the C IV doublet and the C IV $\lambda 1550$ line-locking is the true reason behind this result. A similar case is visible in the leftmost panel, where both components of the O VI $\lambda 1037$ feature overlap with the C II $\lambda 1036$ and O I $\lambda 1039$ ones, resulting in a C II $\lambda 1036$ line-locking stronger than the respective line, contrary to the other transitions. In conclusion, some equivalent widths can be contaminated by these effects and yield unreliable measurements. Relevant (strong) transitions potentially affected by degeneracies are H I $\lambda 949$, O VI $\lambda 1037$, O I $\lambda 1039$, C II $\lambda 1036$, and the C IV $\lambda \lambda 1548, 1550$ doublet. Instead, the Lyman-alpha transition, i.e., H I $\lambda 1215$, and the doublets N V $\lambda \lambda 1238, 1242$ and Si IV $\lambda \lambda 1393, 1402$ will be well-measured in most of our composite spectra.

The line-depth ratios between the line-locking and line features of Figure 6 vary broadly between ~ 0.3 and ~ 0.8 , and the scatter increases when considering more lines. This result suggests that line locking occurs in a fraction of quasar outflows, the exact number depending on the uncertain value of the ratio, which can also be (partially) driven by differences between the optical depths of the line and the line locking. From the composite spectra of about 19 500 narrow ($< 200 \text{ km s}^{-1}$) C IV absorbers in SDSS quasars showing BALs, Bowler et al. (2014) inferred that 50 – 75 % of C IV systems in outflows are line locked, which broadly agrees with our ratio values.

5.2. O VI and N V Line Locking

We search here for line-locking signatures of the O VI and N V doublets, which may have been washed out in our C IV-BAL composite spectra. These ions may potentially participate in the radiative acceleration process through line locking given their high cosmic abundances and the similar strength of their absorption features compared to that of C IV (see, e.g., Figure 6 or the strong effects by these ions already suggested on the quasar spectrum of Figure 3). This argument is also supported by the results by Bowler et al. (2014), who modeled the photoionization state of quasar outflows and found that the optical depths for O VI and N V are similar to that of C IV (their Figure 12). Furthermore, an additional line optical-depth autocorrelation analysis by the same authors confirmed the importance of these two ions to the overall opacity, al-

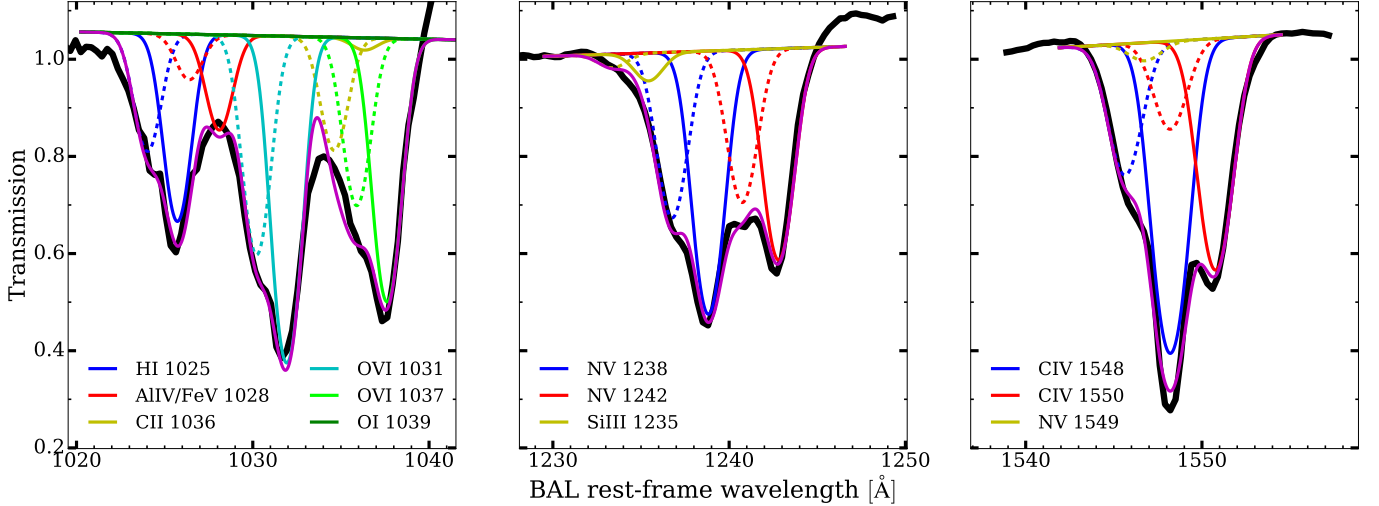


FIG. 6.— Fits to the strongest absorption features in the composite spectrum of the subsample with outflow velocity $1500 \leq v < 3000 \text{ km s}^{-1}$ (spectrum in Figure 5). The *colored solid curves* denote the fit to the individual lines, and the *dashed lines* are the fits to the corresponding line-lockings, following the same color code. The *magenta curves* represent the total fit in each panel. The CIV line-locking components are visibly required to obtain good fits.

though no absorption signatures were detected in their work.

We compute the number of pairs of CIV troughs in our BAL catalog that are separated by a distance from 100 to 2500 km s^{-1} in steps of 50 km s^{-1} . If line locking from other species occurs with frequency, and its signature is strong, the number of troughs at the locking separation should be larger than at other distances. Figure 7 shows the results of this calculation, where we have allowed for different offset values from the exact position of the expected troughs. The dashed vertical lines denote the separations of the NV, OVI, and SiIV doublets. No excess in the number of troughs at the line-locking separations is detected in any case.

We conclude from this analysis that the NV, SiIV and OVI line-locking effects, if present, are not frequent and/or strong enough to produce an absorption feature detectable in the BOSS spectra.

6. DISCUSSION

We discuss the reality of the CIV line-locking features in § 6.1, and possible causes for the non-detection of line locking from other species in § 6.2

6.1. Is It Really Line Locking?

The presence of a CIV line-locking-like feature on the blue side of almost all the absorption lines is apparent in our stacks, but we found no conclusive evidence for the existence of the OVI, NV or other line-locking effects. We revisit here the effects of our methodology that may compromise the reality of the CIV line-locking.

In § 3.2 we checked that centering the BAL spectra at the position of the minimum flux within the absorption troughs yields the most refined (spectrally-resolved) composite spectra. This result is consistent with the findings by Perrotta et al. (2018) and suggests that the origin of the minimum-flux is mostly physical, i.e., due to the presence of the stronger absorption component among the BAL trough, and not driven by noise. In the case of one single CIV doublet, the blue (shorter wavelength) line is expected to be within one and two times stronger

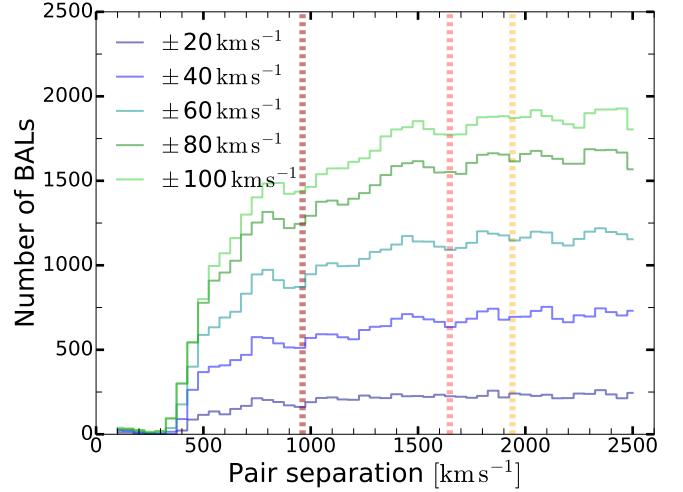


FIG. 7.— Number of pairs of CIV BAL troughs separated by a given distance, from 100 to 2500 km s^{-1} , in steps of 50 km s^{-1} . We enable five offset values from the nominal positions of the troughs. The vertical dashed lines indicate the distances corresponding to the separations of the NV (962 km s^{-1}), OVI (1648 km s^{-1}), and SiIV (1940 km s^{-1}) doublets. No excess in the number of troughs is detected at the line-locking separations.

than the red line, the exact value set by atomic physics (i.e., by the ratio between the two oscillator strengths) and the level of saturation of the lines. In a noise-free doublet therefore, the minimum flux will always appear at the position of the blue line, except in the cases where the two lines are saturated and have the same minimum flux. Thus, although the minimum flux can be mostly governed by the lines, in cases of strong saturation these minima can be identified at the position of the red line of the doublet, with the corresponding location of the blue line at the position of the expected line-locking component. If this occurs a large number of times, a residual feature can be visible in the stacks. Furthermore, the effect of high noise levels could contribute to increase this problem.

We analyze the aforementioned potential impacts from the noise and the strength of the absorption lines be-

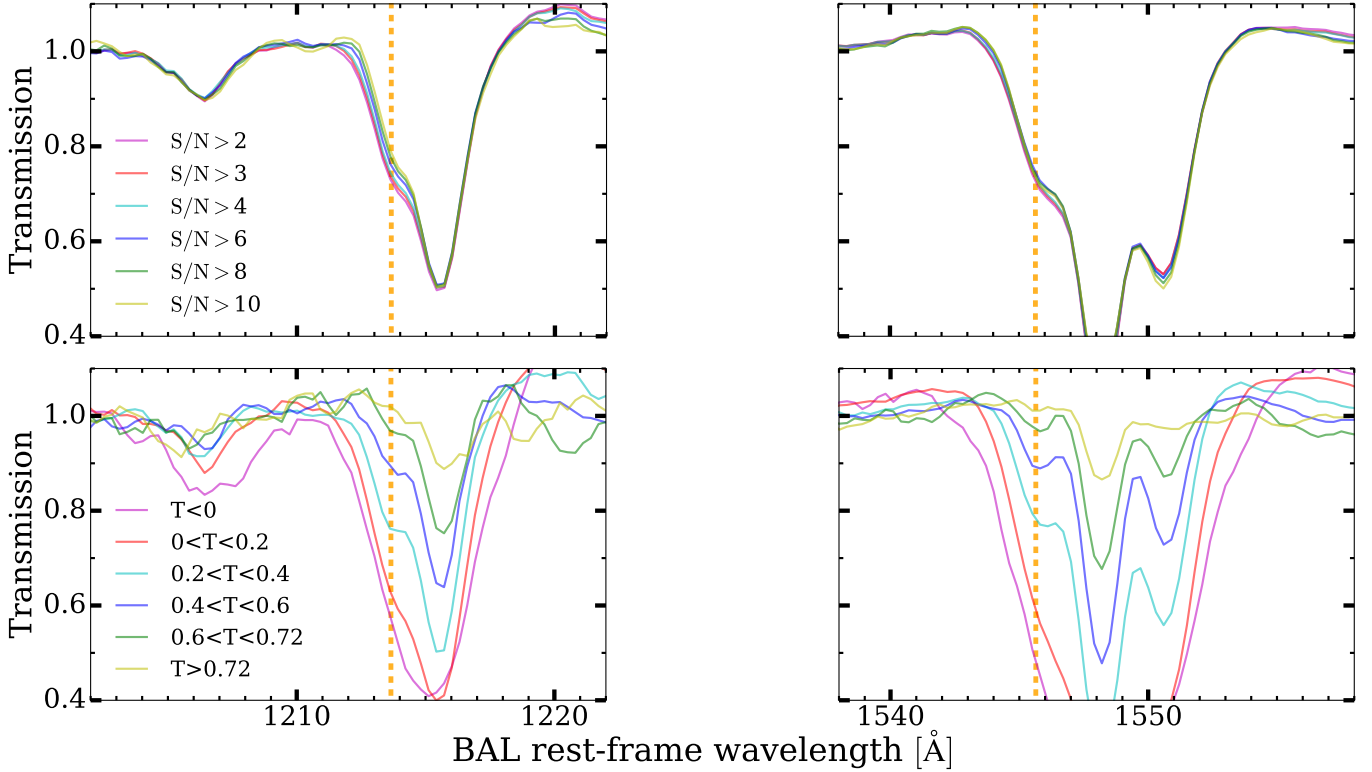


FIG. 8.— Comparison of composite spectra drawn from the BAL subsample with outflow velocity $1500 \leq v < 3000 \text{ km s}^{-1}$ and considering different S/N thresholds (given for the whole spectrum in DR12Q; *upper panel*), and minimum-flux values (transmission) in the BAL troughs (values from the DR12QBAL; *lower panel*). The *left and right panels* illustrate the regions blueward the rest-frame absorption Ly α and CIV doublet features, and the *dashed lines* denote the position of the CIV line-locked components. The line-locking feature is visible in all cases which suggests that it is real and not an artifact from the combination of doublets centered at different lines of the CIV doublet due to the noise or line strength.

low. Figure 8 shows the comparison of composite spectra drawn from the BAL subsample with outflow velocity $1500 \leq v < 3000 \text{ km s}^{-1}$, considering different S/N thresholds (given for the whole spectrum in DR12Q; *upper panel*), and minimum-flux values (transmission) of the BAL troughs (values from the DR12QBAL; *lower panel*). The *left and right panels* illustrate the regions blueward the rest-frame absorption Ly α and CIV doublet, respectively, and the *dashed lines* denote the position of the CIV line-locked components. The *top panels* show that the line-locking features remain almost constant when increasing the S/N of the spectra, reflecting the small impact of the noise on our stacks. The line-locked features are also visible for the different ranges of transmission in the *bottom panels*, indicating the almost negligible effect from strong saturation that could increase the fraction of minimum-flux positions derived from the red line of the doublets. More important, the ratios between the lines and line-lockings remain almost the same in all cases, highlighting the relation between the two components driven by the line-locking effect.

We conclude that the absorption features detected blueward of the absorption lines in our composite BAL spectra is the result of the CIV line-locking effect, which demonstrates the significant contribution from radiation to the acceleration of quasar outflows.

6.2. On the Non-detection of NV and OVI line-locking

It is possible that physical effects do prevent line locking from NV and OVI to occur. Overionization of the

medium inhabited by these species can suppress radiative acceleration from these species since it results in too low opacities and optically thin media (Murray et al. 1995; Chelouche & Netzer 2003; Leighly 2004; Proga & Kallman 2004; Proga 2007a; Laor & Davis 2014; Wang et al. 2015). However, CIV has a lower ionization potential and typically traces cooler and denser media than the oxygen and nitrogen ions. This region could also be shielded (by the highest ions themselves) from the high-energy radiation field and thus enable radiative acceleration from CIV line locking to take place. We will discuss the potential impact of the outflow properties and its structure on the presence of the NV and OVI absorption features in Mas-Ribas et al. (in prep.).

The existence of OVI, NV and other line-locking signatures would be best assessed by using absorption troughs of these species directly identified in the individual quasar spectra instead of using those of CIV. The search for NV and OVI troughs, however, is difficult as they are in regions of the quasar spectrum affected by the Ly α emission line and forest, respectively. Searching for SiIV features may be easier since a fraction of them will likely reside in the line-free region of the rest-frame quasar spectrum. However, the strength of this doublet is significantly smaller than those of OVI, NV and CIV (Fig. 1), and so its line-locking feature could also be weak and difficult to detect. A catalog of SiIV absorption troughs recently built by Guo & Martini (2019) will enable such a calculation. Alternatively, an autocorrelation analysis in the real BOSS spectra may reveal the

characteristic distances where absorption troughs are located, although this requires obtaining the continuum for each individual quasar spectrum with precision, including the region within the Lyman-alpha forest where the continuum is difficult to obtain (Faucher-Giguère et al. 2008a). We defer these calculations to future work.

7. CONCLUSION

We have built 36 outflow composite spectra by stacking broad ($> 450 \text{ km s}^{-1}$) absorption line (BAL) systems in the spectra of SDSS-III/BOSS DR12 quasars. We have computed the composites considering bins in outflow velocity, width of the BALs, degree of detachment between the troughs and the quasars, and quasar redshift and brightness. For every spectrum, we modeled the absorption profiles considering the line and line-locking components of more than 200 atomic transitions. This atomic dataset is publicly available at <https://github.com/lluism/BALs>. Our results can be summarized as follows:

- An absorption feature is visible on the blue side of all the strong absorption lines and in all our 36 composite spectra. This feature is well fitted assuming that it is the CIV line-locking component of the respective absorption lines, at a distance of 497 km s^{-1} from them corresponding to the CIV doublet separation.
- The detectability of the CIV line-locking feature compared to that of the line does not depend on the signal-to-noise of the spectra or the depth of the BAL troughs, indicating that the locking feature is real.
- We investigate the presence of line-locking features from the doublets of OVI, SiIV and NV, but we obtain no detections for these species.
- Our composite spectra resolve the two lines of the CIV and other doublets although the mean width value of the troughs in the stacks is $\approx 2000 \text{ km s}^{-1}$. This implies that (1) the position of the minimum flux in the absorption troughs, which we use for centering our stacks, has a physical meaning (likely representing the blue line of the CIV doublet), and (2) the broad absorption troughs consist on the superposition of narrow absorbers, in agreement with previous findings.

Our results indicate that radiative acceleration is a common mechanism intervening in quasar outflows, and that its presence depends weakly on the characteristics of the winds. Models and simulations assessing the connection between the outflows and AGN feedback should, therefore, incorporate radiative transfer processes that account for the coupling between radiation and the gas,

especially the resonant scattering of photons. The omnipresence of line locking in different wind conditions also suggests that radiative acceleration might be a dominant effect in other environments. These could be the outflows from gamma-ray bursts (Castro-Tirado et al. 2010), quasar jets (Gravity Collaboration et al. 2017), or Seyfert galaxies (Leighly et al. 1997), where line locking has been suggested and tentative detections have been reported. Finally, the fact that line locking is observed for the CIV doublet but not for other species may be connected to the physical properties of a characteristic multiphase structure in the outflow, where different species trace different regions. We will present and test this hypothesis in more detail in a companion paper.

ACKNOWLEDGEMENTS

The initial inspiration for this work grew out of a stimulating discussion with Paul Martini during a visit supported by the Visitor Program at the Ohio State Center for Cosmology and Astroparticle Physics. We are grateful to him for valuable ideas and comments on our paper, and to the CCAP for kind hospitality. We thank Ainar Drews, Mattia Mina, Robert Wissing and Håvard T. Ihle for discussions on line-locking and statistical aspects, and Tzu-Ching Chang, Olivier Doré, Phil Berger, Sterl Phinney, Lee Armus, Ski Antonucci, Brice Ménard, Jordi Miralda Escudé, Sijing Shen, Johan Fynbo, Joop Schaye, Jason X. Prochaska, Bill Forman and Christine Jones for enriching conversations and suggestions. We also thank Signe Riemer-Sørensen for many useful discussions on quasar continua. L.M.R. is grateful to the UCSB/MPIA ENIGMA group for their kind hospitality and, together with other colleagues at JPL and Caltech, for many inspiring discussions during this work. This research was partially carried out at the Jet Propulsion Laboratory, California Institute of Technology, under a contract with the National Aeronautics and Space Administration.

Funding for SDSS-III has been provided by the Alfred P. Sloan Foundation, the Participating Institutions, the National Science Foundation, and the U.S. Department of Energy Office of Science. The SDSS-III web site is <http://www.sdss3.org/>. SDSS-III is managed by the Astrophysical Research Consortium for the Participating Institutions of the SDSS-III Collaboration including the University of Arizona, the Brazilian Participation Group, Brookhaven National Laboratory, Carnegie Mellon University, University of Florida, the French Participation Group, the German Participation Group, Harvard University, the Instituto de Astrofísica de Canarias, the Michigan State/Notre Dame/JINA Participation Group, Johns Hopkins University, Lawrence Berkeley National Laboratory, Max Planck Institute for Astrophysics, Max Planck Institute for Extraterrestrial Physics, New Mexico State University, New York University, Ohio State University, Pennsylvania State University, University of Portsmouth, Princeton University, the Spanish Participation Group, University of Tokyo, University of Utah, Vanderbilt University, University of Virginia, University of Washington, and Yale University.

REFERENCES

- Arav, N., & Begelman, M. C. 1994, *ApJ*, 434, 479
- Arav, N., & Li, Z.-Y. 1994, *ApJ*, 427, 700

- Baldwin, J. A. 1977, *ApJ*, 214, 679
- Barnes, D. J., Kannan, R., Vogelsberger, M., & Marinacci, F. 2018, *ArXiv e-prints*, arXiv:1812.01611
- Baskin, A., Laor, A., & Stern, J. 2014, *MNRAS*, 445, 3025
- Bowler, R. A. A., Hewett, P. C., Allen, J. T., & Ferland, G. J. 2014, *MNRAS*, 445, 359
- Braun, E., & Milgrom, M. 1989, *ApJ*, 342, 100
- Burbidge, E. M., & Burbidge, G. R. 1975, *ApJ*, 202, 287
- Castro-Tirado, A. J., Møller, P., García-Segura, G., et al. 2010, *A&A*, 517, A61
- Cavaliere, A., Lapi, A., & Menci, N. 2002, *ApJL*, 581, L1
- Chelouche, D., & Netzer, H. 2003, *MNRAS*, 344, 233
- Ciotti, L., Ostriker, J. P., & Proga, D. 2010, *ApJ*, 717, 708
- Davies, F. B., Hennawi, J. F., Bañados, E., et al. 2018, *ArXiv e-prints*, arXiv:1801.07679
- Dawson, K. S., Schlegel, D. J., Ahn, C. P., et al. 2013, *AJ*, 145, 10
- Eisenstein, D. J., Weinberg, D. H., Agol, E., et al. 2011, *AJ*, 142, 72
- Faucher-Giguère, C.-A., Lidz, A., Hernquist, L., & Zaldarriaga, M. 2008a, *ApJ*, 688, 85
- Faucher-Giguère, C.-A., Prochaska, J. X., Lidz, A., Hernquist, L., & Zaldarriaga, M. 2008b, *ApJ*, 681, 831
- Foltz, C. B., Weymann, R. J., Morris, S. L., & Turnshek, D. A. 1987, *ApJ*, 317, 450
- Furlanetto, S. R., & Loeb, A. 2001, *ApJ*, 556, 619
- Gabel, J. R., Arav, N., & Kim, T.-S. 2006, *ApJ*, 646, 742
- Ganguly, R., Masiero, J., Charlton, J. C., & Sembach, K. R. 2003, *ApJ*, 598, 922
- Gravity Collaboration, Petrucci, P.-O., Waisberg, I., et al. 2017, *A&A*, 602, L11
- Gunn, J. E., Carr, M., Rockosi, C., et al. 1998, *AJ*, 116, 3040
- Gunn, J. E., Siegmund, W. A., Mannery, E. J., et al. 2006, *AJ*, 131, 2332
- Guo, Z., & Martini, P. 2019, *arXiv e-prints*, arXiv:1901.04506
- Gupta, N., Srianand, R., Petitjean, P., & Ledoux, C. 2003, *A&A*, 406, 65
- Haiman, Z., & Bryan, G. L. 2006, *ApJ*, 650, 7
- Harrison, C. M. 2017, *Nature Astronomy*, 1, 0165
- Harrison, C. M., Costa, T., Tadhunter, C. N., et al. 2018, *Nature Astronomy*, 2, 198
- Hopkins, P. F., & Elvis, M. 2010, *MNRAS*, 401, 7
- King, A., & Pounds, K. 2015, *ARAA*, 53, 115
- Korista, K. T., Voit, G. M., Morris, S. L., & Weymann, R. J. 1993, *ApJS*, 88, 357
- Kramida, A., Yu. Ralchenko, Reader, J., & and NIST ASD Team. 2018, *NIST Atomic Spectra Database* (ver. 5.5.6), [Online]. Available: <https://physics.nist.gov/asd> [2018, August 17]. National Institute of Standards and Technology, Gaithersburg, MD.
- Laor, A., & Davis, S. W. 2014, *MNRAS*, 438, 3024
- Leighly, K. M. 2004, *ApJ*, 611, 125
- Leighly, K. M., Mushotzky, R. F., Nandra, K., & Forster, K. 1997, *ApJL*, 489, L25
- Levine, R., & Gnedin, N. Y. 2005, *ApJ*, 632, 727
- Lu, W.-J., & Lin, Y.-R. 2018a, *MNRAS*, 474, 3397
- . 2018b, *ApJ*, 863, 186
- Lucy, L. B., & Solomon, P. M. 1970, *ApJ*, 159, 879
- Lynds, C. R. 1967, *ApJ*, 147, 396
- Mas-Ribas, L., Miralda-Escudé, J., Pérez-Ràfols, I., et al. 2017, *ApJ*, 846, 4
- Milne, E. A. 1926, *MNRAS*, 86, 459
- Moe, M., Arav, N., Bautista, M. A., & Korista, K. T. 2009, *ApJ*, 706, 525
- Murray, N., Chiang, J., Grossman, S. A., & Voit, G. M. 1995, *ApJ*, 451, 498
- Mushotzky, R. F., Solomon, P. M., & Strittmatter, P. A. 1972, *ApJ*, 174, 7
- Nestor, D., Hamann, F., & Rodríguez Hidalgo, P. 2008, *MNRAS*, 386, 2055
- North, M., Knigge, C., & Goad, M. 2006, *MNRAS*, 365, 1057
- Palanque-Delabrouille, N., Yèche, C., Borde, A., et al. 2013, *A&A*, 559, A85
- Pâris, I., Petitjean, P., Aubourg, É., et al. 2012, *A&A*, 548, A66
- Pâris, I., Petitjean, P., Ross, N. P., et al. 2017, *A&A*, 597, A79
- Perrotta, S., D’Odorico, V., Hamann, F., et al. 2018, *ArXiv e-prints*, arXiv:1808.09995
- Planck Collaboration, Ade, P. A. R., Aghanim, N., et al. 2016, *A&A*, 594, A13
- Prochaska, J. X., Tejos, N., Crighton, N., et al. 2016, *linetools/linetools*: Second major release, doi:10.5281/zenodo.168270
- Proga, D. 2007a, *ApJ*, 661, 693
- Proga, D. 2007b, in *Astronomical Society of the Pacific Conference Series*, Vol. 373, *The Central Engine of Active Galactic Nuclei*, ed. L. C. Ho & J.-W. Wang, 267
- Proga, D., & Kallman, T. R. 2004, *ApJ*, 616, 688
- Proga, D., & Waters, T. 2015, *ApJ*, 804, 137
- Ross, N. P., Myers, A. D., Sheldon, E. S., et al. 2012, *ApJS*, 199, 3
- Scannapieco, E., & Oh, S. P. 2004, *ApJ*, 608, 62
- Scargle, J. D. 1973, *ApJ*, 179, 705
- Smee, S. A., Gunn, J. E., Uomoto, A., et al. 2013, *AJ*, 146, 32
- Srianand, R. 2000, *ApJ*, 528, 617
- Srianand, R., Petitjean, P., Ledoux, C., & Hazard, C. 2002, *MNRAS*, 336, 753
- Wang, T., Yang, C., Wang, H., & Ferland, G. 2015, *ApJ*, 814, 150
- Waters, T., & Proga, D. 2016, *MNRAS*, 460, L79
- Williams, R. E. 1972, *ApJ*, 178, 105